

Quantum Mechanical and Quantum Mechanical/Molecular Mechanical Studies of the Iron–Dioxygen Intermediates and Proton Transfer in Superoxide Reductase

Patrick H.-L. Sit,^{*,†,‡} Agostino Migliore,^{†,‡,§} Ming-Hsun Ho,^{†,‡} and Michael L. Klein^{†,||}

Department of Chemistry, University of Pennsylvania, Philadelphia, Pennsylvania 19104-6323, School of Chemistry, Tel Aviv University, Tel Aviv 69978, Israel, and Institute for Computational Molecular Science, Temple University, Philadelphia, Pennsylvania 19130

Received November 14, 2009

Abstract: Classical and quantum-chemical computations are employed to probe the reaction intermediates and proton-transfer processes in superoxide reductase (SOR) from *Desulfoarculus baarsii*. Ab initio studies of the SOR active site, as well as classical and QM/MM MD simulations on the overall enzymatic reaction, are performed. We explore the use of a Hubbard U correction to standard density functional theory (DFT) in order to obtain a better description of the strongly correlated d electrons in the transition-metal center. The results obtained from the standard and Hubbard- U -corrected DFT approaches are compared with those obtained using different hybrid-DFT functionals. We show that the Hubbard U correction gives a significant improvement in the description of the structural, energetic, and electronic properties of SOR. We establish that adopting the Hubbard U correction in the QM/MM approach leads to increased accuracy with essentially no additional computational cost. Our results suggest that Lys⁴⁸ is one of the likely sources of the first proton donation to the superoxide, either directly or through an interstitial water molecule. Our QM/MM calculations highlight the important role of the interactions and hydrogen-bond network created by the imidazole rings of the His ligands and the internal water molecules. Whereas the hydrogen-bonding pattern due to internal waters can facilitate the protonation event, the interactions with the His ligands and the hydrogen bonds with water can stabilize the dioxygen ligand in a side-on conformation, which, in turn, prevents the immediate proton transfer from Lys⁴⁸, as indicated by recent experimental studies.

Introduction

The interaction of dioxygen species with transition-metal-containing proteins is important in many biological processes including transport, metabolism, respiration, and cell protection. Adventitious reduction of O₂ by redox-active enzymes can yield potentially harmful species such as superoxide, peroxide, hydroperoxide, and hydroxyl radicals, which are inevitably encountered by organisms exposed to molecular

oxygen.¹ In fact, it has been established that both aerobic² and anaerobic³ organisms developed specific mechanisms to protect themselves from oxygen radical species.

The toxicity of the molecular oxygen radicals present on the surface of Earth is a major topic in modern biology and biochemistry, with evident medical significance.⁴ For instance, high levels of superoxide (O₂^{•−}) species are implicated in a number of diseases and neurological disorders,⁵ including diabetes,⁶ Parkinson's^{7,8} and Alzheimer's^{9,10} diseases, and death and tissue damage following a stroke or heart attack.¹¹ It also seems that damage to DNA due to the superoxide radical induces mutations leading to some types of cancer.^{12,13}

* Corresponding author e-mail: sit@sas.upenn.edu.

† University of Pennsylvania.

‡ These authors contributed equally to this work.

§ Tel Aviv University.

|| Temple University.

In the past three decades, research in the field of oxygen toxicity has been focused mainly on three issues:⁴ (i) identification of toxic species, biological targets, and molecular mechanisms of oxidative stress; (ii) understanding of the nature and operation of the antioxidant machinery employed by living organisms for an appropriate balance between generation and scavenging of oxygen radicals in a transitory (anaerobes) or continuous (aerobes) way; and (iii) determination of the effects of oxidative stress on aging and the above-mentioned diseases, as well as the identification and design of suitable therapeutic strategies.

Until the 1990s, the scavenging of superoxide by dismutation to molecular oxygen and hydrogen peroxide, catalyzed by the enzyme superoxide dismutase (SOD),² was considered to be the only biological mechanism for superoxide detoxification. However, it has recently been discovered³ that some anaerobic bacteria and archaea, which might be accidentally exposed to molecular oxygen, protect against harmful oxygen compounds not only by means of SOD, but also through a different class of metalloenzymes, named superoxide reductases (SORs).³ Such enzymes selectively reduce O_2^- species to hydrogen peroxide, without formation of molecular oxygen as a byproduct.⁵ SORs show great efficiency in scavenging O_2^- . Furthermore, by shuttling electrons between auto-oxidizable soluble redox proteins and the superoxide, SORs can simultaneously eliminate O_2^- and the source of its production, also shutting off transient superoxide production without the need for sophisticated regulatory systems.⁴ Such features can play a crucial role in the future development and utilization of SOR mimics,¹⁴ as effective alternatives to SOD mimics, in the therapeutic treatment of the above-mentioned diseases.

The above issues have recently attracted increasing attention within the fields of biochemistry, biology, and medicine. It has been generally suggested that two protonation steps are essential to convert superoxide to hydrogen peroxide. However, the source of the protons, as well as the relation between protonations and the reduction process, are still under debate. Understanding of the SOR mechanism, and thus its control, requires a deep theoretical analysis of the necessary protonation steps and related electron-transfer processes, with special attention to the pertinent energetics and its connection to subtle structural rearrangements. In this work, we present a computational study of the SOR enzymatic mechanism that aims at maximizing the predictive capabilities through the combined use of different theoretical—computational techniques.

Specifically, we first perform a detailed quantum-mechanical (QM) study of the enzyme active site. Next, the behavior of the overall protein system is investigated by means of molecular dynamics (MD) simulations, which are able to capture the most probable scenarios for the two protonation steps involved in the SOR mechanism. Finally, a more accurate description of the overall system is achieved through the quantum-mechanical/molecular-mechanical (QM/MM)^{15,16} approach, where the accuracy of the QM treatment of the enzyme active site can be combined with the speed of the MM computation of the protein framework.

The geometry and energetics of the SOR active site are studied using various hybrid-density functional theory (DFT) schemes and a DFT approach where the exchange-correlation (XC) functional is improved through the introduction of a self-consistent^{17,18} Hubbard- U ¹⁹-corrected electron—electron interaction term. In fact, although DFT computational approaches generally offer the best compromise between accuracy and feasibility for investigating highly correlated many-electron systems,²⁰ they can still suffer from shortcomings related to the approximate character of any currently available XC functional. The use of disparate DFT implementations permits some conclusions to be reached about geometry and electronic structure features of the active site that are robust against the individual computational schemes. This holds at each stage of the SOR enzymatic mechanism, which is characterized by two protonation steps and different scenarios for the pertinent protonation paths. From a computational point of view, our results validate the adopted Hubbard- U -corrected DFT approach and support its use in QM/MM investigations. From a chemical point of view, our results help clarify the nature of the protonation steps, the nonproduction of iron—oxo radicals, and the role of the interstitial water that forms hydrogen bonds between the crucial residue Lys⁴⁸ (see below) and the dioxygen species.

Aims and Methods

SOR Structure and Enzymatic Mechanism: Open Questions. The SOR structure, including the dioxygen moiety, was drawn from the PDB file with the code 2J13.¹ It corresponds to the mutant E114A (Glu¹¹⁴ → Ala¹¹⁴) of SOR from the sulfate-reducing bacterium *Desulfoarculus baarsii*.²¹ The mutation does not alter the overall protein structure, as reported in ref 21 and confirmed by our simulations, but stabilizes the iron—dioxygen complexes relative to the wild-type enzyme. It has been suggested²¹ that the mutation stabilizes the reaction intermediates by avoiding assisted release of hydrogen peroxide by Glu¹¹⁴. The structure of the native reduced enzyme was drawn from the PDB file with the code 2J12.²¹

The asymmetric unit in SOR-E114A crystals includes four monomers, denoted A–D in Figure 1A. Diffraction data collected upon soaking with H_2O_2 are consistent with the formation of end-on (η^1) peroxide species in monomers B–D, whereas monomer A did not show reactivity.²¹ The SOR catalytic domain displays an immunoglobulin-like fold.^{22,23} The active site is made up of an iron atom coordinated to four equatorial histidines and one axial cysteine (Figure 1B), with a vacant sixth coordination site that is exposed to the solvent and available for superoxide binding.²⁴

The SOR catalytic cycle proposed in ref 21 is illustrated in Figure 2. The overall reaction starts with the superoxide binding to a reduced penta-coordinated active site (1) to form the iron—dioxygen complex (2). The first protonation leads to the formation of the iron—hydroperoxo complex (3). After the second protonation of the proximal oxygen atom and electron transfer from the iron to the dioxygen, hydrogen peroxide is formed, and the active site is in its oxidized state

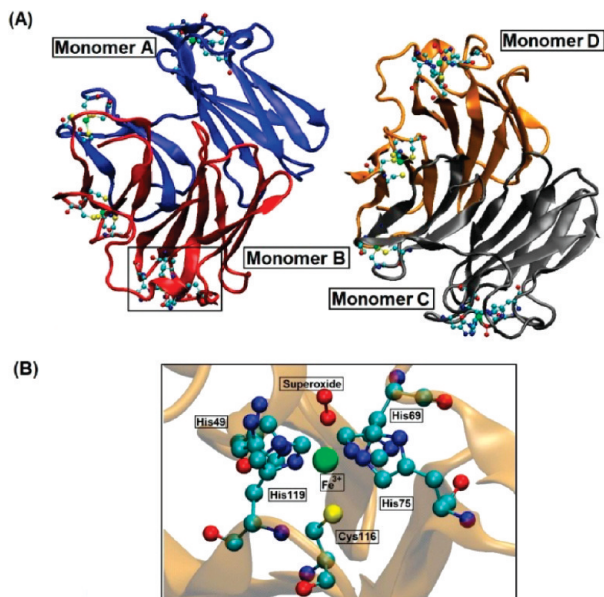


Figure 1. (A) SOR enzyme tetramer. (B) Inset illustrating the active site of monomer B with bound superoxide.

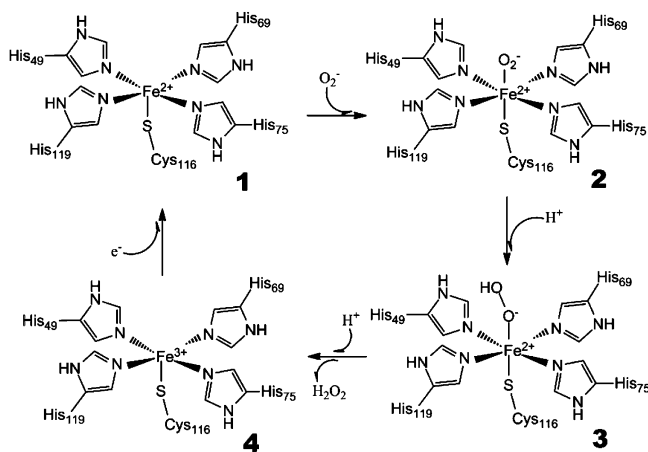


Figure 2. Proposed mechanism for superoxide reduction by SOR.

(4). Finally, the active site is regenerated to its reduced state (1) by an external reducing agent.

The unprotonated peroxo species at step 2 (Figure 2) could correspond to a high-spin side-on (η^2) configuration, as suggested by experiments,^{25–27} but this has not been confirmed by theoretical studies.^{21,28} In iron–dioxygen complexes, the total spin is given by the sum of the electron spins on iron and dioxygen. Evidence indicates that the total spin state is a decisive factor in modulating the strength of the Fe–O and O–O bonds in iron–dioxygen complexes.^{5,29} In fact, some studies have suggested that SORs involve a high-spin ($S = 5/2$) state of the iron,^{25–27} contrary to many heme-containing catalysts that involve low-spin iron states and promote the cleavage of the O–O bond. However, other studies have shown that the ground state corresponds to an intermediate ($S = 3/2$)³⁰ or low ($S = 1/2$)²⁸ spin state. Indeed, the relative stability of the active-site spin states is expected to be strongly affected by the protonation state and the environment. Furthermore, finely tuned electron donation by the Cys¹¹⁶ ligand is expected to precisely adjust the strength

of the Fe–O bond.⁵ Thus, an accurate theoretical study of the electronic distribution in the active site and the corresponding spin state, for the initially unprotonated and subsequent differently protonated intermediates of the iron–dioxygen complex, is crucial to the understanding of the dynamics of the catalytic cycle. In this way also, the connection between the protonation state of the enzyme intermediate and the spin state of the SOR–peroxide complex can be determined.

According to ref 21, the X-ray models of SOR monomers B–D show end-on iron–dioxygen species in three different conformers. Moreover, previous DFT calculations on model SOR active sites based on the X-ray structures favored high-spin end-on (η^1) hydroperoxo species protonated at the distal oxygen, which is consistent with the analysis of pulse-radiolysis data²¹ and is confirmed by the present work. In fact, our DFT calculations allow the energy ordering of the various spin states of the enzyme active site to be established consistently, in correspondence with the active site's different protonation states.

Several issues emerging from recent experimental and theoretical analyses, and partially sketched above, need to be addressed or better understood: (i) the effective proton source in each protonation step; (ii) the exact role of the water molecules and Lys⁴⁸, as well as the conformation of the flexible loop bearing the latter, in those steps; (iii) the nuclear configuration and electronic structure of the iron–dioxygen species, in relation to the protonation state and protein environment; and (iv) the role of the electron donation by the trans thiolate ligand. A deeper understanding of the above points and more predictive capability of the catalytic activity require an accurate QM study of the active site. The effects of the protein and solvent environment and the protein dynamics during the enzymatic reaction can be appreciated using classical molecular dynamics (MD) and the popular composite QM/MM approach.^{15,16} The latter combines the accuracy of the QM treatment of the active site with a classical force-field-based molecular mechanical (MM) treatment of the protein.

QM Study of SOR Active Site. The first focus is on a detailed DFT study of the SOR active site at the different stages of the enzymatic catalytic activity, corresponding to zero, one, and two additional H^+ ions in the active zone. After the pruning of the surrounding protein, we obtained the $Fe^{II}(Im_4MeS)$ model system (Figure 3), where Cys¹¹⁶ was replaced by a methyl thiolate and the four His ligands were replaced by four neutral imidazole rings. Only the oxygen and hydrogen atoms were allowed to move in most of our geometry optimizations of the active site.

Because of the presence of the imidazole rings and the transition metal, electron correlation plays an important role in determining the electronic properties of the system. Hence, DFT offers the best compromise between accuracy and feasibility for a comprehensive study of the enzyme active site. Furthermore, DFT allows the quality of the protein pruning to be checked through calculations on larger atomic models that are unmanageable for extensive study with post-HF approaches, which is also a crucial point in view of the QM/MM calculations discussed later in this article.

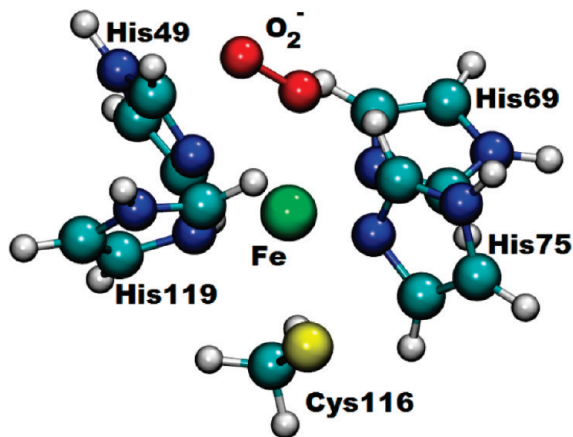


Figure 3. Model of the SOR active site, used in the DFT calculations, including the superoxide moiety (red), iron (green), sulfur (yellow), and imidazole rings (N in blue and C in cyan).

Disparate DFT schemes were adopted, including both plane-wave (PWscf code from the Quantum-Espresso distribution³¹) and atomic (NWChem package³²) basis set approaches. PWscf calculations use the PBE functional³³ in conjunction with Vanderbilt ultrasoft pseudopotentials³⁴ to represent the atomic cores. The energy cutoffs for the plane-wave expansions of the Kohn–Sham spin orbitals and the electron charge density are 30 and 240 Rydberg (Ry), respectively. The self-consistent PBE + U computational scheme^{17,18} described in the next subsection was also employed to provide an improved description of the strongly correlated electron charge around the transition-metal center.

The quantum chemical calculations using localized basis sets were performed with various hybrid XC functionals and, thus, with different amounts of exact Kohn–Sham exchange. The consistency of the results supports the robustness of our conclusions (e.g., as to the energy ordering of the intermediate- and high-spin states), against the approximations differently affecting any currently available XC functional, and especially the unphysical self-interaction arising from the fact that the approximations to the unknown exact functional are independent of the electrostatic repulsion term. Indeed, hybrid XC functionals are conceived in such a way that they cover part of the electron self-interaction error and its long-range correlation effects in a balanced manner.³⁵ As a result, they often perform better than DFT schemes specifically corrected for self-interaction. Furthermore, correcting for the residual self-interaction error does not necessarily improve the ability to reproduce various molecular properties.³⁵ Specifically, we employed the B3LYP,^{36,37} PBE0,³⁸ B97-3,³⁹ and Becke half-and-half⁴⁰ (here denoted by BHH) XC functionals, along with the 6-31+G* Pople-style basis set for the superoxide radical anion and the 6-31G* basis set for the other atoms. In fact, our computational tests indicate that the inclusion of diffuse basis functions has significant effects only regarding the O_2^- moiety.

Ab Initio PBE + U Scheme. The appropriate description of the electron–electron interactions, and thus of their correlations, is a major issue in all quantum chemical calculations. Within DFT, the above-mentioned shortcomings can significantly affect the resulting electron density. An

improved description of the valence electron density can be achieved by adding an orbital-dependent correction functional E_U , adapted from the Hubbard model,¹⁹ to the standard XC functional E_{DFT} . According to the Hubbard- U -corrected DFT approach, a few localized orbitals (specifically, the d-like orbitals around the iron center for the system under consideration) are selected, and the corresponding electron correlation is treated in a special way. The magnitude of E_U , and hence the size of the correction term, is controlled by the U parameter, which gives the strength of the screened on-site Coulomb interactions. The total energy functional is written as

$$E_{DFT+U}[n] = E_U[\{n_{mm'}^{Is}\}] + E_{DFT}[n] \quad (1)$$

where I is the atomic site that experiences the Hubbard-like interaction, s is the electronic spin, m is the magnetic quantum number, and \mathbf{n}^{Is} is the atomic orbital occupation matrix. \mathbf{n}^{Is} describes the degrees of freedom associated with the strongly correlated electrons, on which the U interaction term acts. A recently developed theoretical method²¹ offers a self-consistent recipe for evaluating the U parameter. Within a rotationally invariant formalism, the U value appropriate for a given system is derived from a linear-response approach that is internally consistent with the definition of the occupation matrix.¹⁸ The resultant expression of the corrective energy functional is¹⁸

$$E_U[\{n_{mm'}^{Is}\}] = \frac{U}{2} \sum_{I,s} \text{Tr}[\mathbf{n}^{Is}(1 - \mathbf{n}^{Is})] \quad (2)$$

The functional in eq 2 introduces a penalty, tuned by the U parameter, for partial occupations of the localized orbitals, thus favoring fully occupied or empty spin orbitals. In fact, a positive term is added to the energy in the presence of fractionally occupied orbitals. Yet, the interaction parameter U used in the self-consistent calculations can be determined essentially from first principles,⁴¹ and it need not be treated as an empirical fitting parameter. Note that the PBE + U computational scheme outlined above can allow a substantial self-interaction correction as a result of a more appropriate description of the strong electronic correlation⁴² due to the presence of the iron and the radical anion.

QM/MM Simulations. QM/MM simulations are performed here with the CP2K code.⁴³ The enzymatic system is divided into two parts: (i) the active-site region, which is treated at the QM level with the Hubbard- U -corrected PBE functional, and (ii) the protein and the surrounding water, which are treated at the MM level, using the AMBER force field. In detail, the QM part of the system includes Fe^{2+} , its ligands (His⁴⁹, His⁶⁹, His⁷⁵, His¹¹⁹, and Cys¹¹⁶), Lys⁴⁸, the superoxide anion, and the water molecules within a radius of 6 Å from the latter. The unit-cell size for the QM system is 18 Å × 22 Å × 22 Å. Goedecker–Teter–Hutter pseudopotentials^{44,45} are used to describe electron and ion interactions. Unlike other DFT packages, CP2K uses dual Gaussian-type and plane-wave basis sets.⁴³ We use a basis set of double- ξ quality for Fe and triple- ξ basis sets for the other atoms. A plane-wave cutoff of 280 Ry is chosen to describe the electronic structure of the system. Link atoms

Table 1. DFT Spin-State Energies (kcal/mol) of the Native Reduced SOR^{a-c}

spin state	method					
	PBE	PBE + <i>U</i>	B3LYP	PBE0	B97-3	BHH
low (<i>S</i> = 0)	23.52	58.65	38.67	50.43	43.26	62.56
intermediate (<i>S</i> = 1)	15.68	34.81	21.40	31.47	27.72	34.81

^a Plane-wave calculations used the PBE XC functional and its self-consistent Hubbard *U* correction (*U* = 6.4 eV), denoted by PBE + *U*. ^b Hybrid-DFT evaluations used the 6-31G* basis set and the indicated hybrid functionals. ^c Energies were measured with respect to the high-spin (*S* = 2) state.

are applied, and the interaction between QM and MM regions is calculated using the procedure described by Laino et al.⁴⁶ The Born–Oppenheimer technique is used to propagate the atoms in the quantum region. The time step for the MD simulation is 0.5 fs. The system is coupled with a Nosé–Hoover thermostat^{47,48} at a 100-fs frequency to achieve constant-temperature simulations.

Results and Discussion

Spin-State Energies of the Native Reduced Enzyme. As mentioned above, the employed minimal model is Fe^{II}(Im₄MeS), and its coordinates were obtained by pruning of the protein structure from the PDB file 2JI2. Monomer B of the protein structure was chosen for this study. Note that the superoxide is absent in the native reduced form of the protein. The dangling bonds were saturated with H atoms, which were then relaxed while keeping the coordinates of the heavy atoms fixed as in the 2JI2 X-ray structure. Table 1 shows the energies of the model system in the low- and intermediate-spin states relative to the energy of the high-spin state. All of the calculations, using both plane-wave and atomic basis sets with disparate XC functionals, give the energy order high- < intermediate- < low-spin state. This conclusion is robust against the quality of the XC functional and the kind of basis set. The use of the Hubbard *U* correction to the PBE functional stabilizes the high-spin state relative to the other two spin states. Indeed, magnetic resonance experiments²⁴ indicate that the high-spin state is strongly favored. From a computational point of view, the increased stability of the high-spin state arising from the special treatment of the strongly correlated electrons with the additional Hubbard *U* electronic interaction matches the results from various hybrid XC functions. The latter generally improve the description of electronic properties, as compared to pure DFT schemes, for the following reasons: (i) The delocalization effects in the exchange are better described, thereby reducing the exaggeration of the nondynamic electron correlation. (ii) Both nondynamic and dynamic electron correlations are heeded in a more realistic and effective way, as a consequence of the fitting against experimental data.³⁵ From our data in Table 1 we conclude that the adopted Hubbard *U* correction to the PBE approximation improves the description of electron correlation effects comparably to hybrid-DFT approaches and in line with the expectations from the currently available experimental evidence. This is accomplished essentially without additional computational

Table 2. Structure and Energetics of the Model O₂[−]-Bound SOR Active Site in Its Three Possible Spin States, as Obtained from DFT Plane-Wave Calculations, at the PBE and PBE + *U* Levels, and from Hybrid-DFT Evaluations, Using the Indicated Functionals along with the 6-31+G* Basis Set for the Superoxide Radical Anion and the 6-31G* Basis Set for the Remaining Atoms

method	spin state	d _{Fe–proximal O} (Å)	d _{O–O} (Å)	∠ _{Fe–O–O} (deg)	energy (kcal/mol)
PBE	<i>S</i> = 1/2	1.83	1.38	128.9	7.49
	<i>S</i> = 3/2	1.85	1.37	129.2	−0.19
	<i>S</i> = 5/2	1.91	1.38	142.8	0.00
PBE + <i>U</i>	<i>S</i> = 1/2	2.08	1.35	127.5	45.36
	<i>S</i> = 3/2	2.30	1.35	122.5	−0.41
	<i>S</i> = 5/2	2.31	1.35	122.9	0.00
B3LYP	<i>S</i> = 1/2	1.95	1.34	128.8	21.07
	<i>S</i> = 3/2	2.20	1.34	125.5	0.33
	<i>S</i> = 5/2	2.18	1.34	128.0	0.00
PBE0	<i>S</i> = 1/2	1.96	1.32	127.7	34.37
	<i>S</i> = 3/2	2.17	1.32	125.2	0.12
	<i>S</i> = 5/2	2.17	1.32	126.7	0.00
B97-3	<i>S</i> = 1/2	1.97	1.32	128.1	30.90
	<i>S</i> = 3/2	2.23	1.33	126.9	23.48
	<i>S</i> = 5/2	2.28	1.32	126.4	0.00
BHH	<i>S</i> = 1/2	1.76	1.37	127.6	75.22 (SC = 13%) ^a
		1.73	1.37	127.7	71.02 (SC = 88%) ^a
	<i>S</i> = 3/2	2.25	1.30	125.7	37.24
	<i>S</i> = 5/2	2.23	1.30	125.9	0.00

^a SC stands for spin contamination.

cost relative to standard DFT, which supports an effective use of the PBE + *U* computational scheme in the QM/MM study of the enzyme.

Structure and Energetics of the Iron–Dioxygen Complex in Different Spin States. The minimal model, including the SOR active site and the superoxide species (see Figure 3), is derived from the X-ray structure of the SOR-superoxide intermediate in the monomer B of the mutant SOR-E114A.²¹ We carried out a geometry optimization for each of the three spin states, by relaxing the superoxide and the hydrogen atoms while keeping the other atoms fixed to their experimental positions. Some important geometric parameters obtained in this work at different computational levels are reported in Table 2. The ab initio *U* value obtained for the iron–dioxygen complex is 7.2 eV. This value is similar to the ones adopted in recent electronic structure calculations on the solvated ferrous–ferric redox couple.⁴² The spin-state relative energies are also shown. The PBE, PBE + *U*, B3LYP, and PBE0 computational levels provide very similar energies for the intermediate-spin (*S* = 3/2) and high-spin (*S* = 5/2) states (as compared with *k_BT* at room temperature), whereas the low-spin state is significantly higher in energy. This energy scheme can be attributed to the exchange interaction, which favors parallel spins for the electrons around Fe. In particular, the energies of the *S* = 3/2 and *S* = 5/2 states are close because they are expected to differ by a spin flipping of the outer electron on the superoxide, with the iron remaining in its high-spin state. This result is in contrast to recent QM and QM/MM studies of related iron–oxo systems such as cytochrome P450^{49,50} in which the iron is found to be in low-spin states. Spin-state energetics is expected to depend strongly on the active-site local environment. Moreover, native reduced SOR is experimentally shown to be in a high-spin state,²⁴ in

agreement with our calculation. Therefore, it is not surprising that the SOR active site iron retains its high-spin character when the correct local environment is considered. In fact, the exchange interaction among the electrons around Fe is much higher than that with the electron charge localized on the O_2^- moiety. On the other hand, for the same reason, the above-mentioned spin flipping will only slightly affect the energy of the iron–dioxygen complex, in favor of its high-spin state. This feature is accurately reproduced by the hybrid B3LYP and PBE0 functionals. Also, the PBE and PBE + U computational schemes are able to grasp the near-degeneracy of the $S = 3/2$ and $S = 5/2$ states. Moreover, all of these functionals catch the antiferromagnetic nature of the electron spins on the iron and on O_2^- in the intermediate-spin state, although to the detriment of an appreciable spin contamination (SC).⁵¹ In other terms, such functionals are able to yield a correct antiferromagnetic character of the charge distribution, although they lead to an overall density affected by SC because of the use of a single-determinant DFT approach and of the approximations in the XC functionals. On the contrary, against the expectations based on the exchange interactions, the intermediate-spin states obtained from the BHH and B97-3 calculations do not correspond to a high-spin Fe (see Table 4, below). As a consequence, these functionals lead to a more appreciable energy difference between the $S = 3/2$ and $S = 5/2$ states, as compared with the B3LYP and PBE0 functionals.

In any case, the main conclusions about the energy ordering of the three spin states achieved in this work appear robust against the use of different XC functionals and their inability to obtain SC-free results for the antiferromagnetic electron density corresponding to a different spatial localization of the spin-up and spin-down electrons around the Fe– O_2 complex. The robustness of the main conclusions against the SC problem is exemplified in Table 2 for the BHH results on the low-spin complex. In fact, the different amounts of SC explored through the BHH functional do not affect the energy order of the electronic spin states. It is worth noting that the BHH calculation with higher SC brings about a lower energy, in agreement with the general expectation that spin-unrestricted techniques can give qualitatively correct energies but wrong densities.⁵¹ Note also that the results regarding the high-spin state (which is used in the molecular dynamics studies) are essentially unaffected by SC.

On the other hand, further analyses are required to conclusively establish accurate values of the relative energies in Table 2. Moreover, contrasting results from the existing literature claim that the intermediate-spin state³⁰ or the high-spin one^{25–28,52} is more stable. The exact description of the antiferromagnetic nature of the electron spin densities around iron and superoxide in the $S = 3/2$ state would require accurate multireference calculations,⁵³ with a severe limitation of the accessible size of the model system, or use of the unknown exact XC functional, which would be able to cover all of the contributions to the nondynamic and dynamic electron correlations.³⁵

The low-spin state is consistently endowed with the highest energy. The difference in energy with the high-spin state is similarly appreciated by the PBE + U scheme and the hybrid

Table 3. Structure and Energetics of a Larger Model System Including the Histidine Beta Carbons^a

method	spin state	d_{Fe-S} (Å)	$d_{Fe-proximal O}$ (Å)	d_{O-O} (Å)	\angle_{Fe-O-O} (deg)	energy (kcal/mol)
PBE	$S = 3/2$	2.40	1.83	1.39	126.3	−0.35
	$S = 5/2$	2.56	1.84	1.37	155.9	0.00
PBE + U	$S = 3/2$	2.58	2.26	1.35	125.7	−0.41
	$S = 5/2$	2.56	2.31	1.35	125.9	0.00
B3LYP ^b	$S = 3/2$	2.51	2.12	1.34	127.3	−0.82
	$S = 5/2$	2.50	2.27	1.34	128.6	0.00

^a Histidine beta carbons were kept fixed during geometry optimization, while all the other atoms are allowed to relax. ^b In the B3LYP calculations, the 6-31+G* and 6-31G* atomic basis sets are used for the superoxide radical anion and the remaining atoms, respectively.

functionals, whereas it appears smaller from the PBE calculations. The Hubbard U correction significantly improves on the geometry as well. The PBE calculations display a significant shortening of the distance between iron and proximal oxygen for all spin states. The systematically shorter Fe–proximal O distance in PBE calculations can be viewed as a consequence of the overhybridization of the electronic spin orbitals in this DFT scheme, which is essentially corrected by the Hubbard U interaction term. Indeed, the latter seems to overcorrect for the small Fe–O distance from PBE, but this point cannot be easily addressed on the basis of the available experimental data, because of the uncertainty in the attribution to the system with or without an additional proton. Nevertheless, the results of this section indicate that the adopted Hubbard U correction brings general agreement with the results from various high-quality hybrid functionals. However, the comparison of structural and spin-state energetics data does not provide a strong case for the use of the Hubbard U correction. In fact, the advantage of adopting the Hubbard U correction becomes apparent when we discuss the spin density analysis and the possible reaction products later in this article.

Table 3 reports the results for a larger model of the SOR active site, where the beta carbons of the histidine ligands were added, suitably saturated, and kept fixed during geometry optimization. All other atoms were allowed to relax. The comparison with the data in Table 2, especially at the PBE + U computational level, essentially corroborates the use of the small model system in all of the following calculations. For the larger model, the B3LYP calculation slightly favors the intermediate-spin state, in agreement with the PBE + U results. This stresses the facts that the high- and intermediate-spin states are essentially degenerate and that their energy difference is, indeed, on the order of the relative changes that can be induced by the choice of the atomic model.

Spin Density Analysis of the SOR–Dioxygen Complex in the Relevant Spin States. Table 4 reports the atomic Löwdin spin population of iron, proximal and distal oxygens, and trans thiolate sulfur in the complex intermediate- and high-spin states, at three levels of DFT approximation using the minimal active-site model. For the intermediate-spin state, pure DFT using the PBE XC functional (first row in the table) substantially underestimates the Löwdin spin densities around the iron atom and the two oxygens compared to the B3LYP

Table 4. Spin Density in the (Small) Model of the SOR Active Site for the Intermediate- and High-Spin States^a

method	q_{Fe}	$q_{\text{proximal O}}$	$q_{\text{distal O}}$	q_{O_2}	q_{S}
Intermediate Spin State					
PBE	2.94	0.02	-0.09	0.07	0.03
PBE + U	3.89	-0.43	-0.54	-0.97	0.02
B3LYP	3.72	-0.39	-0.53	-0.92	0.07
High Spin State					
PBE	3.76	0.49	0.40	0.89	0.12
PBE + U	3.88	0.48	0.54	1.02	0.02
B3LYP	3.77	0.49	0.51	1.00	0.06

^a Löwdin spin-up minus spin-down populations (q) on iron, oxygens, and sulfur are reported.

calculation. Such a discrepancy can also be visualized in Figure 4 and corresponds to a migration of spin-up electron charge toward the dioxygen. On the contrary, the spin density from the PBE + U approach shows excellent agreement with that from B3LYP, thus further supporting the supposition that the Hubbard U electron–electron interaction corrects for orbital overhybridization.

The three computational schemes yield similar atomic Löwdin spin populations for the high-spin complex (Figure 5), although they correspond to different spatial distributions. In fact, the net spin density on the dioxygen moiety has a σ^* character according to the PBE results and a π^* character according to the PBE + U and B3LYP calculations. Moreover, the two spin states differ only in the relative spin directions on iron and dioxygen (cf. Figures 4 and 5), in agreement with the discussion in the previous section.

According to both the PBE + U and B3LYP approaches, the dioxygen carries a net spin-up minus spin-down charge of about +1 and -1 in the high-spin and intermediate-spin state, respectively. The change in the sign of the electron spin density corresponds to the electron spin flipping

described above. The absolute value of the spin population, which is around unity in both the spin states, indicates that the superoxide is not reduced to the peroxide species (O_2^{2-}) as a mere consequence of its binding to the protein active site. This is also confirmed by the O–O bond length reported in Tables 2 and 3 for different computational levels. As shown below, the reduction process is likely to occur at a later stage of the enzymatic cycle, where it is assisted by proton transfer.

Peroxide Intermediate after the First Protonation. The protonation steps play an essential role in superoxide reduction. According to Nivière et al.,⁵⁴ the second intermediate in the enzyme reaction cycle is an iron–hydroperoxo complex, which is formed after one proton transfer to the dioxygen ligand. We studied the intermediate by means of DFT calculations on the same active site considered above with the addition of a H^+ ion. Structure optimizations were performed for the $S = 3/2$ and $S = 5/2$ states through plane-wave calculations at the PBE and PBE + U levels and atomic-basis-set calculations using the B3LYP hybrid functional. We obtained the ab initio Hubbard U values of 7.6 and 6.7 eV for the iron–hydroperoxo complex with high and intermediate spin, respectively. Thus, we assumed the same average U value of 7.2 eV for the comparison of the spin-state energies. Only oxygens and hydrogens were allowed to move relative to the crystal structure during geometry relaxation. As for the nonprotonated system, the inclusion of the imidazole beta carbons and the relaxation of the other heavy atoms do not significantly affect any of the main conclusions concerning structure and energetics.

In agreement with previous DFT studies,^{21,28} we consistently find, at different computational levels, that the first protonation occurs at the distal oxygen, irrespective of the

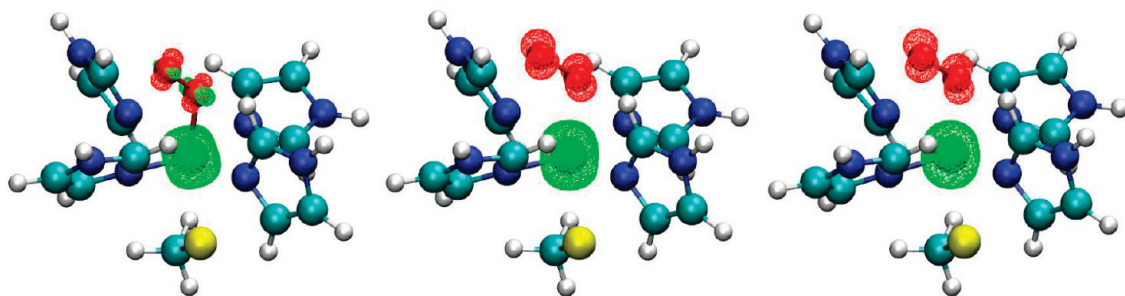
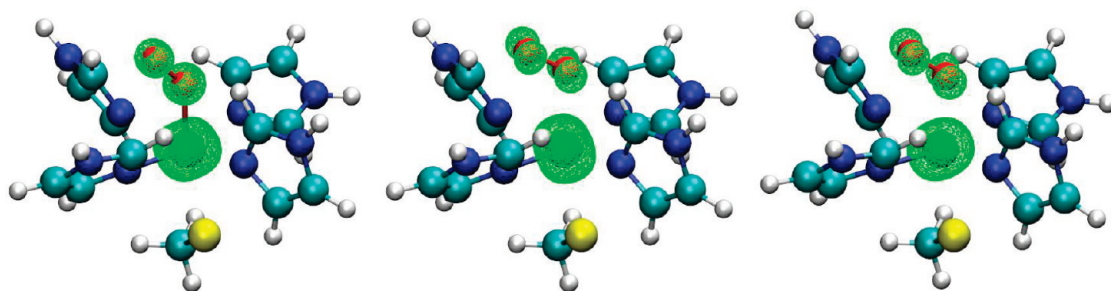
**Figure 4.** Spin density contours for the iron–dioxygen complex in the intermediate-spin state, from (left) PBE, (middle) PBE + U , and (right) B3LYP calculations. The positive and negative isovalues are shown in green and red, respectively.**Figure 5.** Spin density contours for the iron–dioxygen complex in the high-spin state, from (left) PBE, (center) PBE + U , and (right) B3LYP calculations. The positive spin population on the dioxygen is displayed by the isocontour in green.

Table 5. Structural Parameters and Relative Energies for the Model Iron–Hydroperoxo Intermediate in Different Spin States, from DFT Calculations at the PBE, PBE + *U*, and B3LYP Levels

method	spin state	$d_{\text{Fe-proximal O}}$ (Å)	$d_{\text{O-O}}$ (Å)	$\angle_{\text{Fe-O-O}}$ (deg)	energy (kcal/mol)
PBE	$S = 3/2$	1.67	1.91	129.8	4.11
	$S = 5/2$	1.99	1.47	124.8	0.00
PBE + <i>U</i>	$S = 3/2$	2.18	1.44	122.2	0.60
	$S = 5/2$	2.11	1.47	121.8	0.00
B3LYP	$S = 3/2$	1.91	1.47	123.9	8.00
	$S = 5/2$	2.00	1.47	123.9	0.00
expt ²¹		2.00		126	

Table 6. Löwdin Spin-up Minus Spin-down Population on Iron, Oxygens, and Trans Thiolate Sulfur in the SOR Active Site for the Intermediate and High Spin States of the Iron–Peroxo Complex

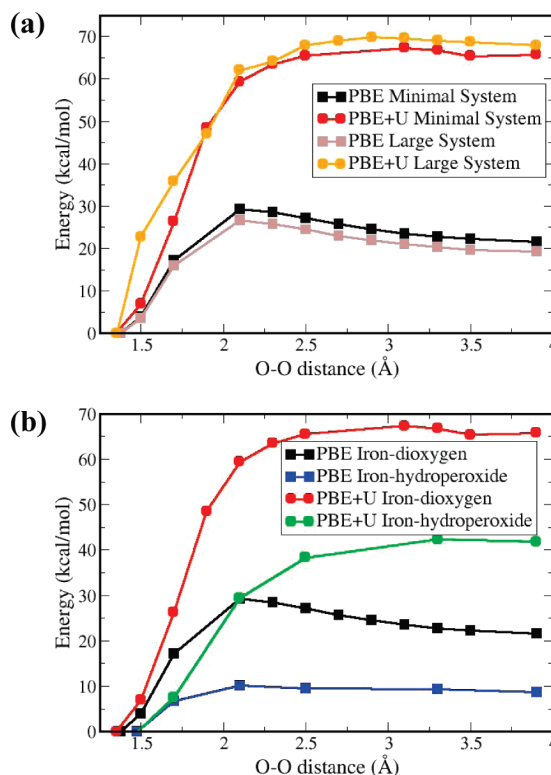
method	q_{Fe}	$q_{\text{proximal O}}$	$q_{\text{distal O}}$	q_{O_2}	q_{S}
Intermediate Spin State					
PBE	3.03	0.21	−0.41	−0.19	−0.04
PBE + <i>U</i>	3.82	−0.31	−0.11	−0.42	−0.36
B3LYP	3.18	0.03	0.00	0.03	−0.29
High Spin State					
PBE	3.97	0.29	0.05	0.34	0.36
PBE + <i>U</i>	4.24	0.22	0.03	0.25	0.27
B3LYP	4.16	0.20	0.03	0.23	0.31

active-site spin state. In fact, proton binding to the proximal oxygen is disfavored by steric hindrance.

Relevant structural parameters and energetics of the iron–hydroperoxo species in SOR, with one additional proton bonded to the distal oxygen, are reported in Table 5. The different computational setups consistently yield a high-spin complex lower in energy than the intermediate-spin one. Note that the O–O bond is broken in the intermediate-spin state from the PBE calculation. Moreover, the O–O bond length has a value typical of peroxide species, which points to its reduction after the first protonation. Therefore, the intermediate-spin and high-spin states mainly differ for the configuration of the electron spins on Fe, rather than for an electron flipping on the dioxygen, which explains the breaking of the quasidegeneracy between the two spin states.

The significant, yet not complete, reduction of the dioxygen after H^+ addition is confirmed by the spin population analysis in Table 6, where the spin-up minus spin-down charge on the peroxide (or, equivalently, on the dioxygen moiety, given that the spin density on the attached hydrogen is negligible) is significantly smaller than the unit electronic charge for all of the XC functionals employed. For both spin states, the PBE data display poor agreement with the B3LYP values. By assuming the B3LYP results as reference values, the adopted Hubbard *U* correction appears not to be effective for the system in the (excited) intermediate-spin state, where the disagreement is rather magnified. On the other hand, the Hubbard *U* correction determines a significant improvement for the high-spin state, which is the relevant one in the SOR catalytic reaction, according to the recent literature.^{21,52}

The comparison between Tables 4 and 6 highlights a donation of spin-down (spin-up) electron charge to the peroxide species from the iron and, through it, from the sulfur

**Figure 6.** Energy profiles for O–O cleavage in the (a) iron–dioxygen and (b) iron–hydroperoxide complexes in the high-spin state, obtained from PBE and PBE + *U* calculations on the two indicated SOR models.

ligand in the high-spin (intermediate-spin) state. In fact, the spin-up minus spin-down populations on iron and sulfur are increased (decreased) and the spin population on the dioxygen moiety is correspondingly decreased (increased), whereas no appreciable changes were obtained in the spin populations of the other atoms. The contribution of the sulfur ligand is an expression of its role in the enzymatic mechanism, which deserves further investigation. The direct contribution from iron indicated by both the PBE + *U* and B3LYP results is larger than that shown by the PBE values.

O–O Bond Cleavage in the Iron–(Hydro)Peroxide Complexes. Unlike heme-based peroxidases and many oxygenases, which promote the cleavage of the oxygen–oxygen bond to form reactive iron–oxo species,^{55–57} SORs form a stable iron–dioxygen intermediate that is subsequently involved in two protonation steps along the catalytic cycle.^{21,25–27} For the system under study, this behavior is well described by the theoretical curves in Figure 6. They were obtained at the PBE and PBE + *U* computational levels and represent the energy profiles of oxygen–oxygen homolysis in the high-spin state of the iron–dioxygen complex, for the two differently sized models of the SOR active site described above. In the minimal model, only oxygens and hydrogens are allowed to move during the geometry optimization at each fixed O–O bond distance, whereas in the larger model, the imidazole beta carbons are kept fixed and the other atoms are relaxed. Figure 6a displays the stability of the iron–dioxygen complex against the cleavage of the O–O bond. The energy barrier for the homolysis obtained by means of the PBE functional is 26.8 kcal/mol. This value

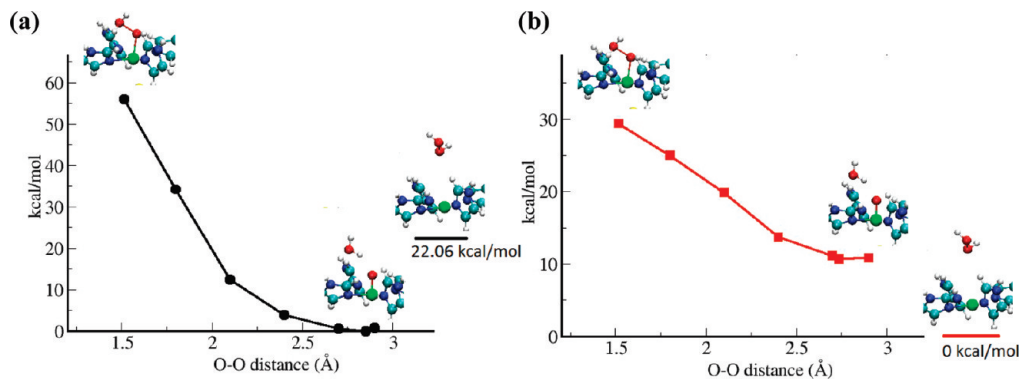


Figure 7. Energy profile for O–O bond cleavage when the H^+ ions are initially bonded to the same oxygen atom, compared to the total energy of the separate active site and hydrogen peroxide, from (a) PBE and (b) PBE + U calculations.

is in good agreement with the value of 24 kcal/mol from a previous study using the B88P86 functional without the Hubbard U correction.⁵⁶ Our PBE + U calculations indicate a stronger stability against O–O bond cleavage, with an energy barrier of 67.8 kcal/mol. The stabilization achieved through the Hubbard U correction can be ascribed to a weakening of the Fe–O interaction after correcting for the PBE overhybridization and a consequent strengthening of the O–O bond. Note that the larger model, where all of the atoms except for the imidazole beta carbons are relaxed, leads to quantitatively similar energy profiles, therefore showing that the relaxation of the ligands does not affect the energetics of the homolysis.

According to previous studies,⁵⁴ the first proton transfer occurs about 100 μs after the formation of the iron–dioxygen complex. It is also suggested,²⁸ and obtained by the present theoretical study, that the distal oxygen is the accepting site for the first protonation. Furthermore, the resulting iron–hydroperoxo complex has to be stable against peroxide cleavage, in order to allow the second protonation step to proceed, leading to hydrogen peroxide formation. This stability was investigated by evaluating the energy profile for the cleavage of the O–O bond in the iron–hydroperoxide complex, as shown in Figure 6b. Calculations were again carried out for the high-spin state. In agreement with the known biology at the SOR active site, our results suggest that the iron–hydroperoxide intermediate is stable after the first protonation process. The added H^+ ion weakens the stability of the molecular oxygen in the SOR active site (compare the blue and green curves with the black and red ones, respectively, in Figure 6b), but the hydroperoxo species is still clearly stable against cleavage. Note that, also in this case, the use of the Hubbard U correction to the PBE computational scheme yields a significant enhancement in the energy barrier against the cleavage of the O–O bond. This can entail a better description of SOR activity through the PBE + U computational approach, given that it matches with the behavior expected from this enzyme.

Second Protonation and Formation of Hydrogen Peroxide. As seen in the previous section, both reaction intermediates are stable against cleavage of the O–O bond. Accordingly, we study the reaction products after two protonations. Two scenarios can be envisaged: (i) In the first case, the second H^+ ion binds to the distal oxygen. This is

expected to lead to the cleavage of the O–O bond and thus to the formation of the iron–oxo reactive complex and a water molecule, similarly to what happens in cytochrome P450. (ii) Alternatively, the second H^+ ion binds to the proximal oxygen, which induces the full reduction of the superoxide to peroxide. Afterward, the hydrogen peroxide leaves the oxidized active site. In fact, the latter is the scenario consistent with the SOR mechanism, in line with experimental evidence.

To test the ability of our computational approach to discriminate between the above scenarios, we performed structural optimizations with the second proton initially attached to either the proximal oxygen or the distal one. The system is kept in the high-spin state, which is shown to be the most stable spin state after both the first and the second protonation, though being almost degenerate with the intermediate-spin state for the iron–dioxygen complex. The same Hubbard U value of 7.2 eV used for the iron–hydroperoxide complex is kept in this study. Indeed, for the oxidized active site and the iron–oxide complex, we obtained self-consistent U values of 7.4 and 7.6 eV, respectively. Therefore, $U = 7.2$ eV, which is quite close to these values, appears to be a convenient choice to study the mechanism of the whole catalytic cycle. The O–O bond breaks, forming a water molecule and an iron–oxide complex if the two protons are both bonded to the distal oxygen. Instead, when the two protons are initially bound to different oxygens, the products are always hydrogen peroxide and the oxidized active site. On the other hand, these final products are lower or higher in energy than the product pair made of the water molecule and the iron–oxide complex according to whether the Hubbard U correction is used or not, respectively. This is illustrated in Figure 7, where we report the energy profile for the O–O bond cleavage when the two H^+ ions are initially bonded to the same oxygen atom, so that oxygen separation is definitely observed along with the total energies of the separate active site and hydrogen peroxide species. Without Hubbard U correction, the water and iron–oxo products are more stable by 22.06 kcal/mol than the hydrogen peroxide and oxidized active-site products. On the contrary, with the Hubbard U correction, the system made of separate hydrogen peroxide and oxidized active site is more stable by 10.72 kcal/mol. Therefore, by introducing the Hubbard U interaction term we can establish the most stable product

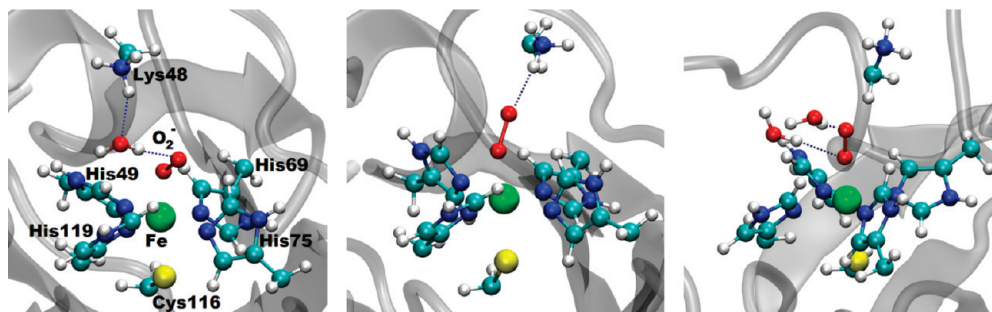


Figure 8. SOR active site in scenarios 1 (left), 2 (middle), and 3 (right).

pair and thus identify the most probable reaction path (i.e., the path starting from single protonations at both the oxygens, which is the only one leading to the expected product pair).

Possible Scenarios for the Proton-Transfer Steps. Our investigation of the possible scenarios for proton transfer to the dioxygen moiety starts with classical MD calculations, using the NAMD simulation package.⁵⁸ The initial configuration was again taken from the experimental X-ray structure¹ (PDB ID 2JI3), but the protein was mutated back to its wild-type form. The AMBER force field (ff03)⁵⁹ was adopted for all of the standard residues, whereas Bloechl charges⁶⁰ were used for the superoxide, Fe^{2+} ion, and its ligands. Harmonic potentials were applied to the metal-ion–ligand coordination. The details of the simulation are discussed in the Supporting Information. The force constants were obtained from our PBE + U calculations on the model active site. The atomic charges and the parameters are also listed in the Supporting Information. The rmsd value along the classical MD simulation, compared to the X-ray structure, is 1.8 Å for the entire-protein heavy atoms and 0.5 Å for the active-site residues. This shows that the overall structure is maintained well with the choice of the force field. The Lys48 residue is relatively flexible and the distance between the N_ζ atom in Lys48 and Fe^{2+} varies from 4.8 to 11.3 Å, with an average distance of 7.76 Å. On the other hand, Glu114 is held more rigidly in the protein matrix, and the distance separating the C_δ atom on the carboxylate group of Glu114 and Fe^{2+} fluctuates between 6.6 and 11.0 Å, with an average value of 8.8 Å.

We explore the corresponding hydrogen-bond networks that can convey proton transfer. A hydrogen bond is defined by the distance and the orientation of hydrogen-bond donor (H–Y) and acceptor (X), with the distance between X–Y smaller than 4.0 Å, and the $\text{X}\cdots\text{H}-\text{Y}$ angle larger than 150° . In scenario 1, the dioxygen is hydrogen-bonded to a single water molecule that, in turn, is hydrogen-bonded to the (protonated) Lys⁴⁸, whereas in scenario 2, the Lys⁴⁸ residue is hydrogen-bonded directly to the superoxide. In scenario 3, only water molecules are hydrogen-bonded to superoxide. Lys⁴⁸ does not form any hydrogen bond with the first water shell of superoxide. The occurrence probabilities for scenarios 1–3 in the classical MD simulation are 11%, 3%, and 34%, respectively. In 52% of the time, the superoxide is not hydrogen-bonded to water or any side chains. Because the formation of hydrogen bonds is the prerequisite for proton transfer, we believe that the most populated scenario in which O_2^- does not form any hydrogen bonds with other species

should not be significant in proton transfer. On the other hand, the average distances between the N_ζ atom in Lys48 and Fe^{2+} are 7.68, 6.79, and 7.47 Å in scenarios 1–3, respectively. Whereas Lys48 comes closer to the metal center to form a direct hydrogen bond to superoxide in scenario 2, Lys48 stays more or less the same distance from the metal center in both scenarios 1 and 3, and the existence of an interstitial water molecule distinguishes the two scenarios.

Quantum chemical studies on the three scenarios were then performed. The model systems for the three representative snapshots from the classical MD represented in Figure 8 were obtained by replacing Cys¹¹⁶ with a methyl thiolate, Lys⁴⁸ with a methyl ammonium, and the four histidines with four neutral imidazole ligands. Only the oxygen and hydrogen atoms were allowed to move during the geometry optimizations. According to our results, in scenarios 1 and 2, proton transfer occurs spontaneously from Lys⁴⁸ to superoxide, either through a water molecule (scenario 1) or directly (scenario 2) in the PBE + U calculations, and there are no barriers in both of these proton transfers. In scenario 3, methyl ammonium was not included in the simulation, because it is not involved in the hydrogen-bond network with the superoxide. We found no proton transfer from the water molecules to the dioxygen during the geometry optimization. In this scenario, Lys⁴⁸ can still be connected to the superoxide through a longer hydrogen-bond chain. Because, in this case, the overall proton-transfer process involves successive hopping steps, the rate of transfer will diminish as the length of hydrogen-bond chain increases. In any case, the quantum chemical calculation for scenario 3 shows that proton transfer from water to superoxide forming a bare hydroxide ion is energetically unfavorable. This, however, does not rule out water as a possible proton source, because the hydroxide ion formed after protonation can be stabilized in the presence of other water molecules from the aqueous environment. B3LYP and PBE0 calculations were also performed at the geometries corresponding to scenarios 1 and 2. They show a proton transfer from Lys⁴⁸ to the superoxide, thus implying that the pK_a of the dioxygen moiety bonded to the SOR active site is higher than that of Lys⁴⁸. Although Lys⁴⁸ is believed to noticeably influence the catalytic activity of SOR, whether its side chain is directly involved in the proton-transfer process is still under debate.^{28,54,61} Moreover, some studies⁵⁴ of the dependence of the protonation rate on the pH suggest that water molecules are mainly involved in the first protonation step. In fact, the first protonation still occurs after K48I mutation, although at a slightly lower rate. This finding

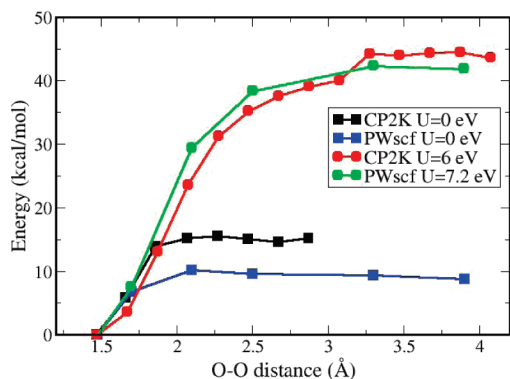


Figure 9. Comparison of the energy profiles for O–O bond cleavage in the iron–hydroperoxide complex, in its high-spin state, obtained using the PWscf program ($U = 0$ and 7.2 eV) and the CP2K code ($U = 0$ and 6 eV).

is partially consistent with our scenario 1, despite the fact that, in our simulations, the ultimate proton source is Lys⁴⁸.

Because scenarios 1 and 2 both occur readily in the classical MD trajectory spanning 60 ns, proton transfer should occur on the nanosecond time scale after the SOR–dioxygen intermediate is formed. However, pulse radiolysis experiments⁵⁴ provide a proton-transfer rate of $(4280 \pm 300) \text{ s}^{-1}$ at neutral pH. Such a huge discrepancy can arise for several reasons. For example, the X-ray structure from which we start our classical MD simulation might be already in the free energy basin that favors the proton transfer. Moreover, our classical MD and subsequent quantum-chemical simulations might have missed some key elements that deter quick proton transfer.

The proton-transfer mechanism was investigated further using the QM/MM approach,¹⁶ which has been demonstrated to be an excellent tool for studying the reactivity of biological systems.^{62,63} The simulation details were provided in the previous section. The high-spin state was chosen for the whole simulation. The occupation matrix used for the Hubbard U implementation in CP2K was obtained by projecting the Kohn–Sham orbitals on a Gaussian basis of d symmetry. Then, the Hubbard U value was chosen in such a way that the structure and energetics of the active site models from CP2K agreed well with the PBE + U results from PWscf. In particular, the energy profiles for the O–O bond cleavage in the iron–hydroperoxo complex from CP2K and PWscf calculations are reported in Figure 9. We find that a U value of 6.0 eV yields an excellent agreement in the energy profile. Furthermore, the spin density obtained with this U value in CP2K (cf. Figures 10 and 5) is essentially the same as that obtained from the PBE + U calculation in PWscf. Specifically, the π -like spin distribution on the dioxygen moiety is correctly reproduced. Moreover, the adopted U value leads to the correct reaction products. In fact, the product pair made of iron–oxo radical and water is more stable than that consisting of oxidized SOR and hydrogen peroxide by 20.51 kcal/mol at the PBE level and is stabilized by 6.93 kcal/mol using the choice of $U = 6$ eV.

The initial configuration for the QM/MM simulation was taken from a snapshot corresponding to scenario 1 in Figure 7. As mentioned above, there is a hydrogen-bond chain

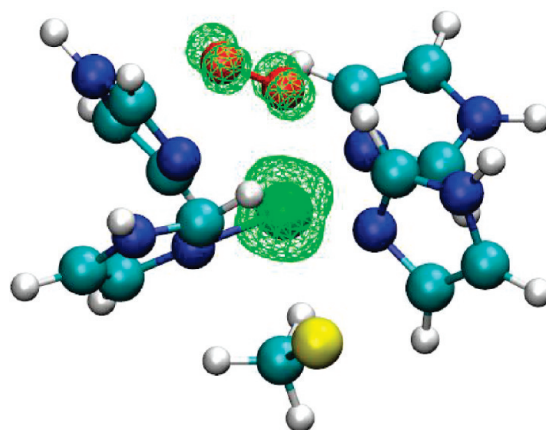


Figure 10. Spin density of the iron–dioxygen complex calculated with PBE + U in CP2K. The positive spin population on the dioxygen is displayed by the isocontour in green.

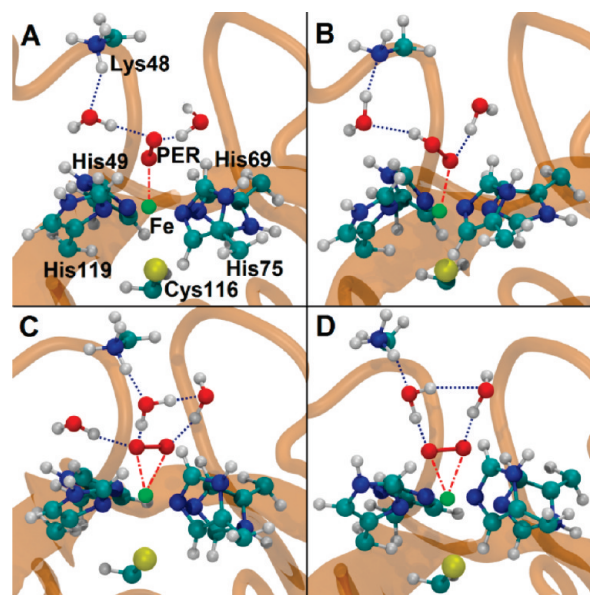


Figure 11. QM/MM simulation starting from (A) a snapshot after 10 ns of classical MD simulation, which is representative of scenario 1. (B) Snapshot after 1 ps of QM/MM simulation showing the proton temporarily transferred to the superoxide. (C) Snapshot taken after 3.5 ps displaying a side-on conformation of the superoxide, which is stably attained and preserved until the end of the simulation (D), at 8.5 ps.

linking Lys⁴⁸, a water molecular, and the O_2^- moiety. We used $U = 6$ eV throughout the MD run and a total simulation time of 8.5 ps. In the first 1.8 ps of simulation, the protons in the hydrogen-bonded chain oscillate between Lys⁴⁸, water, and O_2^- . Parts A and B of Figure 11 show two representative snapshots at 0 and 1 ps, respectively. However, the O_2^- moiety never permanently captures the proton from the hydrogen-bond chain. Instead, after about 1.8 ps, it adopts a side-on conformation, as shown in Figure 11C. There is no proton oscillation along the hydrogen-bond chain after the side-on conformation is attained, and protonation does not occur for the rest of the MD simulation (see Figure 11D).

Whereas our quantum calculations on the model active site from the crystal structure²¹ in the various spin states always give a stable conformation of the end-on type, our

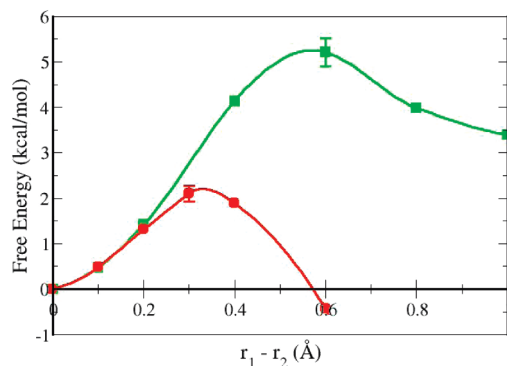


Figure 12. Free energy profile from side-on to end-on conformation from CP2K calculations with a Hubbard U value of 6.0 eV. The conformational rearrangement corresponding to the red curve is accompanied by a proton transfer from Lys⁴⁸ to the superoxide. The green curve was obtained by restraining the H⁺ on Lys⁴⁸, in order to isolate the conformational change from the protonation step.

QM/MM study stabilizes the side-on configuration, as also suggested by the studies on the natural enzyme^{27,52} and biometric models.^{64,65} According to our QM/MM results, the side-on dioxygen conformer hinders fast proton transfer. We performed thermodynamic integrations⁶⁶ by constraining $r_1 - r_2$, where r_1 and r_2 are the Fe–O_{distal} and Fe–O_{proximal} distances, respectively. Each window was simulated for at least 3 ps after equilibration was attained. We thus obtained the free energy profile connecting the side-on and end-on conformations. As shown in Figure 12 (red curve), we obtained a barrier of ~2.3 kcal/mol in going from the side-on to the end-on complex. When the O–O moiety is pushed end-on in the free-energy calculation, the proton transfer occurs immediately, suggesting a barrierless transition. The value for the height of the energy barrier is of the same order of magnitude as its estimate from the experimental proton-transfer reaction rate⁵⁴ using the transition-state theory, which is about 10 kcal/mol. The actual comparison with experiment needs to consider that the proton donation from Lys⁴⁸, which accompanies the conformational rearrangement in our QM/MM simulation, can be hindered by displacements of the flexible loop bearing Lys⁴⁸. The energy profile for the transition from the side-on to the end-on conformation without proton transfer is represented by the green curve in Figure 12, which was obtained by making the proton sources, that is, Lys⁴⁸ and the surrounding water molecules, rigid.

To understand why QM/MM suggests a different stable conformation than that obtained from our QM calculations on the model active site from the SOR crystal structure, we constructed the model active site from the system structure after 3.5 ps of QM/MM simulation (see Figure 11C), by including the Lys⁴⁸ residue and the relevant water molecules around the active site. In this snapshot, the side-on O₂[−] is hydrogen-bonded to the His imidazoles and to the water molecules, which, in turn, are hydrogen-bonded to Lys⁴⁸. The orientations of the His ligands differ from those in the crystal structure and appear to stabilize the side-on dioxygen conformer. This stabilization does not correspond to a significant increase of the Fe–imidazole distances, as claimed in a recent theoretical study.²⁸ In fact, we calculated the

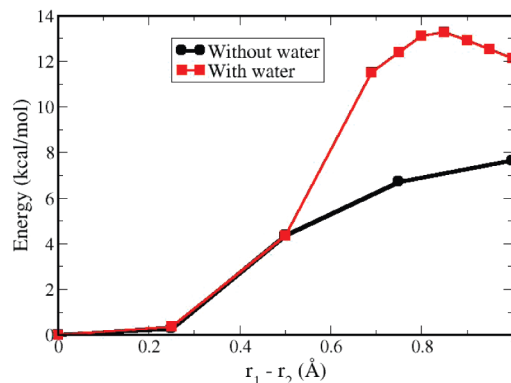


Figure 13. Energy of the end-on conformer, relative to the side-on conformer, against the $r_1 - r_2$ internal coordinate, with (red) and without (black) interstitial water.

average distance between Fe and the four His ligand nitrogen atoms from our QM/MM simulation and found only a 0.03 Å increase compared to the experimental structure.²¹ Note that fixing the heavy atoms to the experimental structure in our gas-phase calculations is not the reason why the side-on conformation was not observed from previous calculations^{21,28} and our calculations involving a larger model system also gave an end-on conformation. Important further stabilization comes from the hydrogen bonds with the surrounding water molecules. The energy of the end-on conformer relative to the side-on conformer is shown in Figure 13 as a function of the $r_1 - r_2$ internal coordinate, which measures the departure from the side-on conformation. The two energy profiles, which were obtained from PBE + U calculations with CP2K on the model active site taken from one QM/MM snapshot, display the stability of the side-on conformer relative to the end-on one. Their difference gives a measure of the contribution to side-on stabilization by waters, even if an exact superposition of the hydrogen bonds to histidines and water molecules is not assumed. Ultimately, our findings point to the stabilization of the side-on superoxide conformer, which is not amenable to protonation according to our calculations, in a significant percentage of the protein conformations as a major motif in justifying the observed rate for the first protonation step of the enzymatic cycle.

Conclusions

Our extensive quantum-mechanical study of the SOR active site through various DFT approaches leads to the following conclusions: (i) In a vacuum, keeping the coordinates of the heavy atoms as in the crystal structure, the end-on conformation of the dioxygen ligand is favored to the side-on one before and after the first protonation step. In general, the dioxygen conformation can depend on the conformation of the active site. (ii) For the iron–dioxygen complex, the quasidegeneracy of the high-spin and intermediate-spin states is rationalized in terms of exchange forces between the dioxygen ligand and the central iron. The first protonation stabilizes the high-spin state and induces a significant reduction of the superoxide. (iii) The main features of the active-site structure and energetics are captured and shown to be robust against different hybrid-DFT schemes, the

standard DFT-PBE approach, and its Hubbard U correction. (iv) The observed electron charge donation from the sulfur ligand to the dioxygen moiety through Fe suggests a specific role for the sulfur ligand that is worthy of further investigation. (v) The adopted Hubbard U correction to the standard DFT-PBE approximation leads to results in general agreement with the high-level hybrid-DFT computational schemes using the B3LYP and PBE0 XC functionals. Moreover, PBE wrongly predicts the reaction products after two protonations, whereas the Hubbard U term corrects for this deficiency. The present results should encourage the use of the correction term in QM/MM calculations, thus allowing the study of the active-site region without additional computational cost as compared with standard DFT.

The use of classical MD allows exploration of possible scenarios for the protonation steps involved in the enzymatic cycle. They are essentially characterized by hydrogen-bond networks that can convey protons toward the dioxygen species. Discrimination among the possible scenarios, as well as their effectiveness in the protonation steps, is gained through a QM/MM approach. The latter provides with the following indications on the SOR mechanism: (i) The Lys⁴⁸ residue is one of the proton sources for the first protonation, either directly or through the interstitial water. (ii) The imidazole rings of the His ligands and the interstitial water afford a pattern of interactions and hydrogen bonds that appears to play an essential role in the enzyme catalytic mechanism. In fact, whereas the hydrogen-bond pathways involving the water molecules could convey protons to the iron–dioxygen complex, the stabilization of the dioxygen moiety in a side-on conformation by the same hydrogen bonds and especially by the interactions with the histidine ligands prevents an immediate proton transfer. This conclusion is, indeed, irrespective of the presence of possible proton sources other than Lys⁴⁸. (iii) We find an energy barrier between the side-on and end-on dioxygen conformations. This barrier is of the correct order of magnitude, as compared with recent experimental findings.

Future work will involve the QM/MM study of scenario 2 and the investigation of whether the active site can afford a side-on dioxygen conformation without the presence of interstitial water molecules. Moreover, the detailed structural change in the active site in response to the formation of the side-on conformer can be fruitfully studied. In particular, it has been shown that the stability of the side-on conformation is related to the Fe–S ligand bond strength.²⁷ Furthermore, wild-type and mutated enzymes show different yields in the side-on conformation. Finally, the first protonation still occurs after the K48I mutation, although at a slightly lower rate, which points to the presence of another proton source in addition to Lys⁴⁸ that needs to be investigated.

The methodology presented and widely tested in this work appears to be a valid tool for the above-mentioned future explorations. Moreover, our present results concerning the chemistry at the SOR active site, and especially the hindrance to the first protonation provided by the side-on dioxygen conformation, offer a contribution to the understanding of the SOR catalytic cycle. In fact, our work might aid in suggesting new mutations useful to control the enzymatic

mechanism. We believe that the Hubbard- U -corrected DFT scheme within the QM/MM approach can be a fruitful approach to handle transition-metal enzymatic systems.

Acknowledgment. We thank the National Institutes of Health for supporting this work under Grant GM067689.

Supporting Information Available: Details of our classical molecular dynamics, atomic charges used in the SOR active site obtained from DFT + U calculations (Table S1), and force field parameters also calculated from DFT + U calculations (Table S2). This material is available free of charge via the Internet at <http://pubs.acs.org>.

References

- (1) Halliwell, B.; Gutteridge, J. *Free Radicals in Biology and Medicine*, 3rd ed.; Oxford University Press: Oxford, U.K., 1999; pp 31–32.
- (2) Mccord, J. M.; Fridovic, I. *J. Biol. Chem.* 1969244 (22), 6049.
- (3) Jenney, F. E.; Verhagen, M. F. J. M.; Cui, X. Y.; Adams, M. W. W. *Science* **1999**, 286 (5438), 306.
- (4) Niviere, V.; Fontecave, M. *J. Biol. Inorg. Chem.* **2004**, 9 (2), 119.
- (5) Brines, L. M.; Kovacs, J. A. *Eur. J. Inorg. Chem.* 2007 (1), 29.
- (6) Maritim, A. C.; Sanders, R. A.; Watkins, J. B. *J. Biochem. Mol. Toxicol.* **2003**, 17 (1), 24.
- (7) Ihara, Y.; Chuda, M.; Kuroda, S.; Hayabara, T. *J. Neurol. Sci.* **1999**, 170 (2), 90.
- (8) Kocatürk, P. A.; Akbostanci, M. C.; Tan, F.; Kavas, G. Ö. *Pathophysiology* **2000**, 7 (1), 63.
- (9) Marklund, S. L.; Adolfsson, R.; Gottfries, C. G.; Winblad, B. *J. Neurol. Sci.* **1985**, 67 (3), 319.
- (10) De Leo, M. E.; Borrello, S.; Passantino, M.; Palazzotti, B.; Mordente, A.; Daniele, A.; Filippini, V.; Galeotti, T.; Masullo, C. *Neurosci. Lett.* **1998**, 250 (3), 173.
- (11) Fortunato, G.; Pastinese, A.; Intrieri, M.; Lofrano, M. M.; Gaeta, G.; Censi, M. B.; Boccalatte, A.; Salvatore, F.; Sacchetti, L. *Clin. Biochem.* **1997**, 30 (7), 569.
- (12) Burdon, R. H. *Free Radical Biol. Med.* **1995**, 18 (4), 775.
- (13) Toh, Y.; Kuninaka, S.; Mori, M.; Oshiro, T.; Ikeda, Y.; Nakashima, H.; Baba, H.; Kohnoe, S.; Okamura, T.; Sugimachi, K. *Oncology* **2000**, 59 (3), 223.
- (14) Shearer, J.; Nehring, J.; Lovell, S.; Kaminsky, W.; Kovacs, J. A. *Inorg. Chem.* **2001**, 40 (22), 5483.
- (15) Warshel, A.; Levitt, M. *J. Mol. Biol.* **1976**, 103 (2), 227.
- (16) Laio, A.; VandeVondele, J.; Rothlisberger, U. *J. Chem. Phys.* **2002**, 116 (16), 6941.
- (17) Cococcioni, M.; Dal Corso, A.; de Gironcoli, S. *Phys. Rev. B* **2003**, 67 (9), 094106.
- (18) Cococcioni, M.; de Gironcoli, S. *Phys. Rev. B* **2005**, 71 (3), 035105.
- (19) Hubbard, J. *Proc. R. Soc. London Ser. A* 1963276 (Dec), 238.
- (20) Nowak, M. J.; Lapinski, L.; Kwiatkowski, J. S.; Leszczynski, J. In *Molecular Structure and Infrared Spectra of the DNA Bases and Their Derivatives: Theory and Experiment*; Leszczynski, J., Ed.; World Scientific: Singapore, 1997; pp 140–216.

- (21) Katona, G.; Carpentier, P.; Niviere, V.; Amara, P.; Adam, V.; Ohana, J.; Tsanov, N.; Bourgeois, D. *Science* **2007**, *316* (5823), 449.
- (22) Adam, V.; Royant, A.; Niviere, V.; Molina-Heredia, F. P.; Bourgeois, D. *Structure* **2004**, *12* (9), 1729.
- (23) Yeh, A. P.; Hu, Y. L.; Jenney, F. E.; Adams, M. W. W.; Rees, D. C. *Biochemistry* **2000**, *39* (10), 2499.
- (24) Clay, M. D.; Jenney, F. E.; Hagedoorn, P. L.; George, G. N.; Adams, M. W. W.; Johnson, M. K. *J. Am. Chem. Soc.* **2002**, *124* (5), 788.
- (25) Bukowski, M. R.; Halfen, H. L.; van den Berg, T. A.; Halfen, J. A.; Que, L. *Angew. Chem., Int. Ed.* **2005**, *44* (4), 584.
- (26) Mathe, C.; Mattioli, T. A.; Horner, O.; Lombard, M.; Latour, J. M.; Fontecave, M.; Niviere, V. *J. Am. Chem. Soc.* **2002**, *124* (18), 4966.
- (27) Mathe, C.; Niviere, V.; Houee-Levin, C.; Mattioli, T. A. *Biophys. Chem.* **2006**, *119* (1), 38.
- (28) Silaghi-Dumitrescu, R.; Silaghi-Dumitrescu, L.; Coulter, E. D.; Kurtz, D. M. *Inorg. Chem.* **2003**, *42* (2), 446.
- (29) Costas, M.; Mehn, M. P.; Jensen, M. P.; Que, L. *Chem. Rev.* **2004**, *104* (2), 939.
- (30) Shearer, J.; Scarrow, R. C.; Kovacs, J. A. *J. Am. Chem. Soc.* **2002**, *124* (39), 11709.
- (31) Quantum-ESPRESSO is a community project for high-quality quantum-simulation software, based on density-functional theory, and coordinated by Paolo Giannozzi. See <http://www.quantum-espresso.org> and <http://www.pwscf.org>.
- (32) (a) Aprà, E.; Windus, T. L.; Straatsma, T. P.; Bylaska, E.; de Jong, W.; Hirata, S.; Valiev, M.; Hackler, M.; Pollack, L.; Kowalski, K.; Harrison, R.; Dupuis, M.; Smith, D. M. A.; Nieplocha, J.; Tipparaju, V.; Krishnan, M.; Auer, A. A.; Brown, E.; Cisneros, G.; Fann, G.; Fruchtl, H.; Garza, J.; Hirao, K.; Kendall, R.; Nichols, J.; Tsemekhman, K.; Wolinski, K.; Anchell, J.; Bernholdt, D.; Borowski, P.; Clark, T.; Clerc, D.; Dachsel, H.; Deegan, M.; Dyall, K.; Elwood, D.; Glendening, E.; Gutowski, M.; Hess, A.; Jaffe, J.; Johnson, B.; Ju, J.; Kobayashi, R.; Kutteh, R.; Lin, Z.; Littlefield, R.; Long, X.; Meng, B.; Nakajima, T.; Niu, S.; Rosing, M.; Sandrone, G.; Stave, M.; Taylor, H.; Thomas, G.; van Lenthe, J.; Wong, A.; Zhang, Z. *NWChem, A Computational Chemistry Package for Parallel Computers*, version 4.7; Pacific Northwest National Laboratory: Richland, WA, 2005.
- (b) Kendall, R. A.; Aprà, E.; Bernholdt, D. E.; Bylaska, E. J.; Dupuis, M.; Fann, G. I.; Harrison, R. J.; Ju, J.; Nichols, J. A.; Nieplocha, J.; Straatsma, T. P.; Windus, T. L.; Wong, A. T. *Comput. Phys. Commun.* **2000**, *128*, 260.
- (33) Perdew, J. P.; Burke, K.; Ernzerhof, M. *Phys. Rev. Lett.* **1996**, *77* (18), 3865.
- (34) Vanderbilt, D. *Phys. Rev. B* **1990**, *41* (11), 7892.
- (35) Cremer, D. *Mol. Phys.* **2001**, *99* (23), 1899.
- (36) Becke, A. D. *J. Chem. Phys.* **1993**, *98* (7), 5648.
- (37) Lee, C.; Yang, W.; Parr, R. G. *Phys. Rev. B* **1988**, *37* (2), 785.
- (38) Adamo, C.; Barone, V. *J. Chem. Phys.* **1999**, *110* (13), 6158.
- (39) Keal, T. W.; Tozer, D. J. *J. Chem. Phys.* **2005**, *123* (12), 121103.
- (40) Becke, A. D. *J. Chem. Phys.* **1993**, *98* (2), 1372.
- (41) Kulik, H. J.; Cococcioni, M.; Scherlis, D. A.; Marzari, N. *Phys. Rev. Lett.* **2006**, *97* (10), 103001.
- (42) Migliore, A.; Sit, P. H. L.; Klein, M. L. *J. Chem. Theory Comput.* **2009**, *5* (2), 307.
- (43) VandeVondele, J.; Krack, M.; Mohamed, F.; Parrinello, M.; Chassaing, T.; Hutter, J. *Comput. Phys. Commun.* **2005**, *167* (2), 103.
- (44) Goedecker, S.; Teter, M.; Hutter, J. *Phys. Rev. B* **1996**, *54* (3), 1703.
- (45) Hartwigsen, C.; Goedecker, S.; Hutter, J. *Phys. Rev. B* **1998**, *58* (7), 3641.
- (46) Laino, T.; Mohamed, F.; Laio, A.; Parrinello, M. *J. Chem. Theory Comput.* **2005**, *1* (6), 1176.
- (47) Nose, S. *J. Chem. Phys.* **1984**, *81* (1), 511.
- (48) Hoover, W. G. *Phys. Rev. A* **1985**, *31* (3), 1695.
- (49) Wang, D.; Thiel, W. *J. Mol. Struct. (THEOCHEM)* **2009**, *898* (1–3), 90.
- (50) Shaik, S.; Cohen, S.; Wang, Y.; Chen, H.; Kumar, D.; Thiel, W. *Chem. Rev.* **2009**, *110* (2), 949.
- (51) Koch, W.; Holthausen, M. C. *A Chemist's Guide to Density Functional Theory*; Wiley: New York, 2000.
- (52) Horner, O.; Mouesca, J. M.; Oddou, J. L.; Jeandey, C.; Niviere, V.; Mattioli, T. A.; Mathe, C.; Fontecave, M.; Maldivi, P.; Bonville, P.; Halfen, J. A.; Latour, J. M. *Biochemistry* **2004**, *43* (27), 8815.
- (53) Jensen, F. *Introduction to Computational Chemistry*, 2nd ed.; John Wiley and Sons Ltd.: Chichester, U.K., 2007; pp 153–159.
- (54) Niviere, V.; Asso, M.; Weill, C. O.; Lombard, M.; Guigliarelli, B.; Favaudon, V.; Houee-Levin, C. *Biochemistry* **2004**, *43* (3), 808.
- (55) Lehnert, N.; Neese, F.; Ho, R. Y. N.; Que, L.; Solomon, E. I. *J. Am. Chem. Soc.* **2002**, *124* (36), 10810.
- (56) Lehnert, N.; Ho, R. Y. N.; Que, L.; Solomon, E. I. *J. Am. Chem. Soc.* **2001**, *123* (51), 12802.
- (57) Decker, A.; Solomon, E. I. *Curr. Opin. Chem. Biol.* **2005**, *9* (2), 152.
- (58) Phillips, J. C.; Braun, R.; Wang, W.; Gumbart, J.; Tajkhorshid, E.; Villa, E.; Chipot, C.; Skeel, R. D.; Kale, L.; Schulten, K. *J. Comput. Chem.* **2005**, *26* (16), 1781.
- (59) Duan, Y.; Wu, C.; Chowdhury, S.; Lee, M. C.; Xiong, G.; Zhang, W.; Yang, R.; Cieplak, P.; Luo, R.; Lee, T.; Caldwell, J.; Wang, J.; Kollman, P. *J. Comput. Chem.* **2003**, *24* (16), 1999.
- (60) Blochl, P. E. *J. Chem. Phys.* **1995**, *103* (17), 7422.
- (61) Emerson, J. P.; Coulter, E. D.; Cabelli, D. E.; Phillips, R. S.; Kurtz, D. M. *Biochemistry* **2002**, *41* (13), 4348.
- (62) De Vivo, M.; Dal Peraro, M.; Klein, M. L. *J. Am. Chem. Soc.* **2008**, *130* (33), 10955.
- (63) Ho, M. H.; Vivo, M. D.; Peraro, M. D.; Klein, M. L. *J. Chem. Theory Comput.* **2009**, *5* (6), 1657.
- (64) Roelfes, G.; Vrajmasu, V.; Chen, K.; Ho, R. Y. N.; Rohde, J. U.; Zondervan, C.; la Crois, R. M.; Schudde, E. P.; Lutz, M.; Spek, A. L.; Hage, R.; Feringa, B. L.; Munck, E.; Que, L. *Inorg. Chem.* **2003**, *42* (8), 2639.
- (65) Girerd, J. J.; Banse, F.; Simaan, A. Characterization and Properties of Non-Heme Iron Peroxo Complexes. In *Metal-Oxo and Metal-Peroxo Species in Catalytic Oxidations*; Springer: Berlin, 2000; pp 145–177.
- (66) Ciccotti, G.; Ferrario, M.; Hynes, J. T.; Kapral, R. *Chem. Phys.* **1989**, *129* (2), 241.